

# Interplay of Chemical, Electronic, and Structural Effects in the Triple-Conducting BaFeO<sub>3</sub>–Ba(Zr,Y)O<sub>3</sub> Solid Solution

Giulia Raimondi, Rotraut Merkle,\* Alessandro Longo,\* Francesco Giannici,\* Olivier Mathon, Christoph J. Sahle, and Joachim Maier



Cite This: *Chem. Mater.* 2023, 35, 8945–8957



Read Online

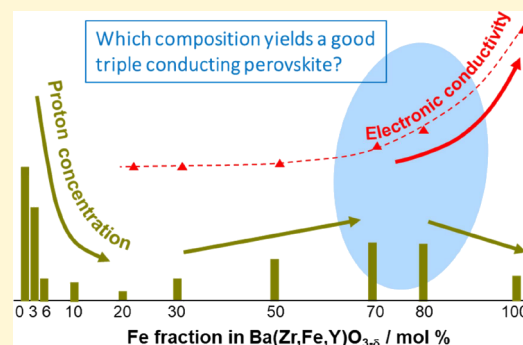
ACCESS |

Metrics & More

Article Recommendations

Supporting Information

**ABSTRACT:** Triple-conducting oxides with mobile protons, oxygen vacancies, and holes are key functional materials for protonic ceramic fuel/electrolysis cells. We comprehensively investigate the Ba(Zr,Y,Fe)O<sub>3-δ</sub> perovskite solid solution series ranging from electrolyte to electrode-type materials depending on iron content. From thermogravimetry and impedance spectroscopy, the proton and oxygen vacancy concentrations as well as electronic and ionic conductivities are determined. X-ray spectroscopy (Fe *K*-edge XANES, O *K*-edge Raman scattering, Fe, Zr, Y *K*-edge EXAFS) elucidates the finer features of the electronic structure and local distortions. A low Fe content of ≤10% strongly decreases the degree of hydration, while comparably high Fe concentrations of ≥70% are required to obtain an electronic conductivity sufficient for an electrode material. The transport of ionic and electronic carriers is interrelated in a complex way and is closely linked to details of the electronic structure (strength of Fe–O hybridization) and geometrical distortions (Fe–O–Fe and Fe–O–(Zr,Y) buckling). As a result, an optimum combination of proton concentration and electronic conductivity is not obtained in the middle of the solid solution series but rather found for Fe-rich materials with 20–30% doping with oversized, redox-inactive cations. A similar behavior is also expected for related solid solutions between a large-band gap electrolyte and small-band gap redox-active perovskites.

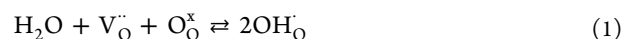


## 1. INTRODUCTION

Hydrogen technologies such as fuel and electrolysis cells are expected to play a prominent role in the transition to a defossilized energy supply. Protonic ceramic fuel/electrolysis cells (PCFC/PCEC) are particularly promising for intermediate-temperature applications due to their advantages over their parent solid oxide fuel/electrolysis cells (SOFC/SOEC). These include a lower operating temperature (400–600 °C), higher fuel utilization in the fuel cell mode, direct production of dry and compressed hydrogen in the electrolysis cell mode, and decreased cost.<sup>1–13</sup>

PCFC/PCEC uses a proton-conducting ceramic electrolyte typically based on the BaZrO<sub>3</sub> perovskite. This is doped with acceptors such as Y<sup>3+</sup> and/or Yb<sup>3+</sup> on the perovskite B-site to induce oxygen vacancies which can be hydrated to form protonic carriers. The composition may be further modified by partial substitution of Zr<sup>4+</sup> with Ce<sup>4+</sup> to improve sintering properties and proton conductivity (14–16 and refs therein). The performance of protonic ceramic cells is largely limited by the kinetics of oxygen reduction or water oxidation, that is, the reactions involving breakage or formation of the O=O double bond. To accelerate the kinetics, the catalytically active zone should extend beyond the three-phase-boundary using a “triple-conducting” electrode material capable of transporting protons, oxygen vacancies, and electron holes.<sup>17–24</sup> Typical

PCFC/PCEC oxygen electrode materials are perovskites with a high Ba content on the A-site and one or more redox-active transition metal ions on the B-site. More complex structures are also investigated; see, for example,<sup>15</sup> and refs therein. These materials typically show *p*-type conductivity and contain oxygen vacancies V<sub>O</sub><sup>•</sup> (or empty O interstitial sites) into which water can dissociatively be incorporated, forming protonic defects OH (hydroxide ion on a regular oxygen lattice site; O<sub>O</sub><sup>x</sup> is a regular oxide ion) according to eq 1:



This is the same reaction that forms protonic carriers in electrolytes, but the latter show a higher degree of hydration (the fraction of available V<sub>O</sub><sup>•</sup> filled with protons).<sup>17,20,25</sup> Solid solutions between large band gap and small band gap barium-based perovskites have been investigated for fundamental interest,<sup>26,27</sup> and attempts have been made to develop

Received: June 20, 2023  
 Revised: October 13, 2023  
 Accepted: October 13, 2023  
 Published: October 31, 2023

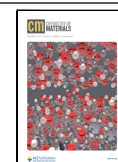


Table 1. Sample Compositions, Abbreviations, Synthetic Route, Sintering Condition, and Pellet Lattice Parameters<sup>a</sup>

sample	stoichiometry	synthesis route	sintering condition	lattice parameters/Å
F0	BaZr <sub>0.88</sub> Y <sub>0.12</sub> O <sub>3-<math>\gamma</math></sub>	MO	1600 °C × 6 h	4.22
F01	BaZr <sub>0.87</sub> Y <sub>0.12</sub> Fe <sub>0.01</sub> O <sub>3-<math>\delta</math></sub>	MO	1600 °C × 6 h	4.21
F03	BaZr <sub>0.85</sub> Y <sub>0.12</sub> Fe <sub>0.03</sub> O <sub>3-<math>\delta</math></sub>	MO	1600 °C × 6 h	4.21
F06*	BaZr <sub>0.82</sub> Y <sub>0.12</sub> Fe <sub>0.06</sub> O <sub>3-<math>\delta</math></sub>	MO	1600 °C × 6 h	4.21
F10*	BaZr <sub>0.78</sub> Y <sub>0.12</sub> Fe <sub>0.10</sub> O <sub>3-<math>\delta</math></sub>	MO	1500 °C × 16 h	4.21
F20	BaZr <sub>0.68</sub> Y <sub>0.12</sub> Fe <sub>0.20</sub> O <sub>3-<math>\delta</math></sub>	MO	1500 °C × 16 h	4.19
F30*	BaZr <sub>0.58</sub> Y <sub>0.12</sub> Fe <sub>0.30</sub> O <sub>3-<math>\delta</math></sub>	MO	1500 °C × 16 h	4.19
F50	BaZr <sub>0.38</sub> Y <sub>0.12</sub> Fe <sub>0.50</sub> O <sub>3-<math>\delta</math></sub>	W	1450 °C × 16 h	4.16
F70*	BaZr <sub>0.18</sub> Y <sub>0.12</sub> Fe <sub>0.70</sub> O <sub>3-<math>\delta</math></sub>	W	1450 °C × 16 h	4.14
F80	BaZr <sub>0.08</sub> Y <sub>0.12</sub> Fe <sub>0.80</sub> O <sub>3-<math>\delta</math></sub>	W	1450 °C × 8 h	4.12
BLF	Ba <sub>0.95</sub> La <sub>0.05</sub> FeO <sub>3-<math>\delta</math></sub>	W	1200 °C × 8 h	4.00

<sup>a</sup>MO, mixed oxide synthesis; W, wet synthesis. Samples indicated with \* underwent oxidation and reduction treatments for X-ray spectroscopy; see Table S1.

electrolytes into triple-conducting PCFC cathode materials.<sup>28–30</sup>

In the present work we investigate the solid solution series BaZr<sub>0.88-x</sub>Fe<sub>x</sub>Y<sub>0.12</sub>O<sub>3- $\delta$</sub>  (0 < x < 0.8) that ranges from electrolyte-type materials for low iron content to electrode-type materials for larger x. The Y addition is chosen to ensure a sufficient V<sub>O</sub><sup>•</sup> concentration also for samples with a low Fe content. For comparison, we also include Ba<sub>0.95</sub>La<sub>0.05</sub>FeO<sub>3- $\delta$</sub>  (5 mol % of La is necessary to keep the cubic structure<sup>31</sup>). Thermogravimetry (TG) and electrochemical impedance spectroscopy (EIS) show that the hydration thermodynamics and the electrical conductivity strongly depend on the iron content, and already a small amount of iron ( $\approx$ 10 mol %) drastically changes the material properties. A comprehensive study of the local and electronic structures using X-ray spectroscopy helps to understand the modification in the hydration and conductivity behavior when going from an electrolyte to an electrode material.

## 2. MATERIALS AND METHODS

**2.1. Powders and Pellet Preparation.** Sample compositions, abbreviations, treatments, and lattice parameters are given in Table 1. Zr-rich sample powders were prepared by solid mixed oxide synthesis,<sup>20,32</sup> while Fe-rich sample powders were obtained from aqueous nitrate solutions using citric acid and ethylenediaminetetraacetic acid complexing agents.<sup>32,33</sup> In both cases, the last step is calcination in air at 1100 °C (mixed oxide synthesis) or 1000 °C (wet synthesis) for 8 h. Since the sintering occurred at high temperatures (mostly 1450–1600 °C, Table 1), the different powder synthesis methods are not expected to affect the final pellet properties. This is supported by the fact that neither lattice parameters (Figure S1) nor proton uptake or electronic and V<sub>O</sub><sup>•</sup> conductivity (Figure 11) show any step-like changes between F30 and F50.

For TG and electrical conductivity experiments, the powders were sintered into pellets with relative densities above 92%. About 2 g of powder was compacted in a 11 mm diameter rubber mold applying an isotatic pressure of 20 kN for 1–2 min. The green pellets were sintered in air using the conditions in Table 1. Phase purity of the samples was checked by XRD (Cu K $\alpha$ , Bragg–Brentano geometry, PANalytical Empyrean). All investigated samples have a cubic perovskite structure (space group *Pm3m*). The fitted lattice parameters from Rietveld refinement (Table 1) follow Vegard's law (Figure S1) indicating that BaZr<sub>0.88-x</sub>Fe<sub>x</sub>Y<sub>0.12</sub>O<sub>3- $\delta$</sub>  is a solid solution.

**2.2. TG.** Proton uptake and oxygen nonstoichiometry were measured using an STA 449C (Netzsch, Germany) instrument with a total gas flow of 60 mL min<sup>-1</sup>. The exhaust was monitored with a quadrupole mass spectrometer (QMS 200 F1, Balzers Prisma, Germany). For TG, the sintered pellets were crushed and sieved into two fractions:<sup>23</sup> (i) 100–250  $\mu$ m particle size for hydration (low

surface area to avoid water surface adsorption, allowing one to kinetically freeze-in the oxygen exchange during the hydration steps). (ii) <100  $\mu$ m for oxygen stoichiometry (smaller particles to shorten the equilibration time for the slow oxygenation reaction described by eq 2).



This reaction describes the incorporation of oxygen into lattice oxygen vacancies, leading to the formation of electron holes (h<sup>•</sup>) which are more or less shared between the transition metal and adjacent oxygen ions.<sup>17,25,34,35</sup> The absolute oxygen stoichiometry is fixed using the fact that at high T and low pO<sub>2</sub>, iron in the BZYF samples approaches the 3+ oxidation state as in related ferrate perovskites.<sup>36</sup>

For hydration, 1–2 g of crushed particles were quenched from 700 °C in dry N<sub>2</sub> to freeze the oxygenation reaction (eq 2). In this way, all iron remain Fe<sup>3+</sup>, thus maximizing [V<sub>O</sub><sup>•</sup>]<sup>20</sup> and obtaining the proton concentration predominantly from the hydration reaction (eq 1). After quenching, isothermal measurements were run at 250–700 °C. The water partial pressure p<sub>H<sub>2</sub>O</sub> was adjusted by feeding dry N<sub>2</sub> gas into a water evaporator at 5, 12, and 18 °C and, if necessary, mixing with dry N<sub>2</sub>. Stepwise changes of p<sub>H<sub>2</sub>O</sub> from dry to maximum humidity (p<sub>H<sub>2</sub>O</sub> = 16.7 mbar) and back confirm the reversibility of the hydration. In isothermal experiments, buoyancy effects are negligible. F0 and F03 are measured in the dynamic mode (cooling from 750 °C with 1.5–0.5 K min<sup>-1</sup>) in wet N<sub>2</sub> (p<sub>H<sub>2</sub>O</sub> = 16.7 mbar), given their high hygroscopicity, which makes it difficult to return to the completely dehydrated state at lower temperatures.

For the oxygen stoichiometry measurements, about 500 mg of sample was measured in dry oxidizing conditions (0.085%, 2.5%, 83.3% O<sub>2</sub>), while the temperature was decreased from 900 to 300 °C with cooling rates of 0.2 to 2.0 K min<sup>-1</sup>. The buoyancy correction was performed by using data from a crucible filled with an appropriate amount of inert alumina.

**2.3. X-ray Spectroscopy.** Samples with fixed oxygen stoichiometry were prepared in order to investigate the behavior as a function of iron formal oxidation state. The choice of the treatment conditions is based on previous experiments.<sup>34,36</sup> The reduction of samples (Fe mainly in 3+ formal oxidation state) was carried out in the TG furnace with 1.5% of H<sub>2</sub> at 700 °C for 4–5 h. The oxidation (Fe mainly 4+) was carried out in an autoclave at 600 bar of pure O<sub>2</sub>, while the temperature was decreased from 550 to 250 °C within 72 h. The success of the treatment is already visible by the color of the powders, which turn brownish after the reduction and black after oxidation (see Figures S3–4). The exact stoichiometry of oxidized samples was checked with TGA either by heating to 900 °C in N<sub>2</sub> or to 700 °C in 1.5% H<sub>2</sub>, and in both cases, a plateau corresponding to the iron being 3+ could be observed; the samples reached at least 96% of their nominal oxygen stoichiometry.

**2.3.1. X-ray Absorption Spectroscopy.** For transmission measurements, the amount of powders required for an edge jump  $>0.1$  absorption length for the respective element was calculated using XAFS mass.<sup>37</sup> For fluorescence measurements, the amount of powder was calculated to be  $10^{19-18}$  atoms of the desired element per  $\text{cm}^2$  of the sample pellet. The weighted amount was premixed in a mortar with the minimum amount of cellulose (nanocrystalline cellulose, Sigma-Aldrich) to obtain a self-standing pellet (ca. 100 mg in total). The mixture was milled in a small volume ball miller (Pulverisette 23, Fritsch, Germany) for 10–15 min and uniaxially pressed into pellets with 3 kN ( $\varnothing$  5 mm pellets) or 10 kN ( $\varnothing$  13 mm pellets) for 5 min. The X-ray absorption spectroscopy (XAS) spectra were collected at BM23-ESRF (European Synchrotron Radiation Facility, Grenoble, France)<sup>38</sup> at 80 or 10 K. The data were collected at the Fe *K*-edge (7.1 keV), Y *K*-edge (17.0 keV), and Zr *K*-edge (17.9 keV). Most measurements were done in transmission, except for F06 and F10, where the Fe *K*-edge was measured in fluorescence. The details of the data treatment and analysis can be found in the Supporting Information.

**2.3.2. X-ray Raman Scattering.** Sample powders were sealed in glass capillaries. All O *K*-edge (520–590 eV) data were collected at ID20 at ESRF. The details of the data collection and treatment can be found in the Supporting Information and are similar to the ones used in ref 35. For the simulations, the starting structures here are  $\text{BaZrO}_3$  (BZ) for the samples below 70 mol % of iron, and  $\text{BaFeO}_3$  (BF) for F70. Also here, we applied the semiempirical parameters *screening* and *dilatorb* to account for the different interactions between the transition metal (TM) *d* and O *2p* orbitals (smaller *screening* = stronger electronic correlation between scattering atom and its environment, typically related to larger hybridization and correspondingly lower oxide ion basicity) and for eventually increased orbital overlap (higher *dilatorb* = larger hybridization because of the bigger atomic orbital overlap).

**2.4. Conductivity Measurements.** Electrical conductivity was measured by EIS using an Alpha-A high-resolution impedance analyzer (Novocontrol, Germany) in the frequency range of typically  $10^6$ – $10^{-2}$  Hz (down to  $10^{-3}$  Hz for ionic conductivity) with a typical 0.02 V amplitude. The electron hole and oxygen vacancy conductivities were measured for F10, F20, F30, F50, F70, and BLF at 700–350 °C. Usually, the Nyquist plots show one semicircle analyzed using a single R-CPE equivalent circuit. In the case of electronic conductivity, especially in high  $p\text{O}_2$ , just a single resistance appeared.

**2.4.1. Electronic Conductivity  $\sigma_{\text{eorr}}$ .** The electronic conductivity was measured by AC impedance spectroscopy in the two-point mode on bars cut from sample pellets, contacted at the end with Ag-paste and Pt-wires as in ref 39. For the majority of samples, it was not required to correct for the resistance of the cables; for F80 and BLSF, the cable resistance reached about 10% of the overall resistance and was subtracted. The impedance spectra were free of any low-frequency semicircle originating from a contact resistance between the sample and the electrode. The samples were equilibrated in dry 100%  $\text{O}_2$ .

**2.4.2. Ionic Conductivity of Oxygen Vacancies  $\sigma_{\text{V}_\text{O}}$ .** Measuring ionic conductivities in this type of sample is challenging because the high electron hole mobility and concentration dominate the conductivity. Nevertheless, the oxygen vacancy conductivity can be obtained by measuring the samples in dry conditions over an extended  $p\text{O}_2$  range, which is achievable by integrating an oxygen pump (Huber Scientific, Austria) in the setup. This allows us to measure EIS in the  $p\text{O}_2$  region  $10^{-10}$ – $10^{-20}$  bar, where the ionic plateau is expected. Fe will completely be in the 3+ oxidation state, and  $\sigma_{\text{V}_\text{O}}$  is independent of  $p\text{O}_2$  because  $[\text{V}_\text{O}^\bullet]$  is fixed. More details are reported in the Supporting Information. The samples used for  $\sigma_{\text{V}_\text{O}}$  are pellets with  $\approx 400$  nm of sputtered Pt (Edwards Auto306, UK) on the large edges for keeping the equilibration time reasonable, and they are spring-loaded between two Pt-foil contacts. In the same setup, bar-shaped samples are also measured in 100, 10, 1, 0.1, and 0.01%  $\text{O}_2$  (yielding  $\sigma_{\text{eorr}}$ ).

## 3. RESULTS AND DISCUSSION

### 3.1. Hydration and Oxygen Nonstoichiometry.

**3.1.1. Proton Uptake.** The hydration behavior measured by TG is shown in Figure 1. The proton concentration

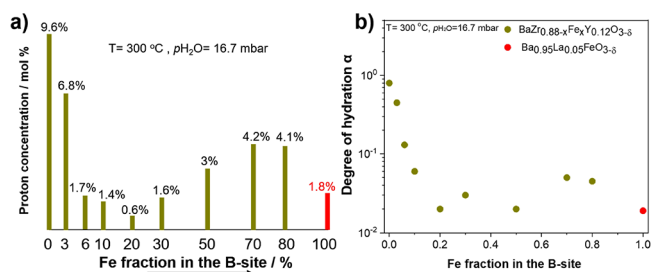


**Figure 1.** (a) Proton concentration and (b) degree of hydration of  $\text{BaZr}_{0.88-x}\text{Fe}_x\text{Y}_{0.12}\text{O}_{3-\delta}$  as a function of iron content in the B-site;  $T = 300$  °C, and  $p\text{H}_2\text{O} = 16.7$  mbar. The BLF data are taken from ref 20. The absolute error bars in (a) are ca. 0.1%, and the corresponding relative errors in the degree of hydration in (b) are 1–15% and thus within the symbol size.

(Figure 1a) decreases strongly by introducing up to 20 mol % of Fe. For further increasing iron content, the proton uptake increases again to approximately 4 mol % for Fe >50 mol %.

The end member BLF deviates from this trend. This is attributed to its lower oxygen ion basicity caused by higher Fe–O bond covalency (less/no local distortions<sup>34,35</sup>) compared with the other samples with dopants on the B-site. The increase in the proton concentration for F50 and F70 appears surprising at first glance, considering that one would expect highly covalent Fe–O bonds there. However, X-ray spectroscopy discussed below demonstrates that the F70 local structure is more distorted than F30 and F10, which decreases the Fe  $\rightarrow$  O hole transfer and thus preserves the oxide ion basicity.<sup>17,34,35</sup>

A trend similar to that for the proton concentration is found for the degree of hydration (Figure 1b). It decreases from almost complete hydration for F03 by 1 order of magnitude already for 10 mol % of iron. This strikingly demonstrates the strongly different hydration behavior of cathode and electrolyte materials, while many  $\text{BaFeO}_{3-\delta}$ -based cathode materials exhibit higher  $[\text{V}_\text{O}^\bullet]$  than typical  $\text{Ba}(\text{Zr,Ce,Y})\text{O}_{3-z}$  electrolytes (Figures 2 and S8). With the room temperature and water partial pressure of  $p\text{H}_2\text{O} \approx 20$  mbar, complete hydration is not achieved, in contrast to electrolytes.<sup>14</sup> A strong decrease of proton uptake upon substitution with several mol % Co has also been observed for  $\text{BaZr}_{0.8-x}\text{Sc}_{0.1}\text{Co}_x\text{O}_{3-\delta}$ .<sup>40</sup>

These strong variations in the hydration behavior also show up in the  $\Delta H_{\text{hydr}}^\circ$  and  $\Delta S_{\text{hydr}}^\circ$  values of typical cathode and electrolyte materials, as summarized in Figure 2.  $\Delta H_{\text{hydr}}^\circ$  and  $\Delta S_{\text{hydr}}^\circ$  for the present materials are calculated from the van't Hoff plots reported in Figures S5–7 and are summarized in Table S2. While a systematic theory of hydration thermodynamics is not available so far, one can hypothesize that it is related to various effects, such as effects from the local geometric and electronic structure. Compared to  $\text{Ba}(\text{Zr,Y})\text{O}_{3-z}$  electrolytes, the  $\Delta H_{\text{hydr}}^\circ$  values are systematically less negative for electrode materials and  $\Delta S_{\text{hydr}}^\circ$  values more negative; both disfavor the hydration.  $\text{Ba}(\text{Ce,Y})\text{O}_{3-z}$  electrolytes show more negative entropies compared to electrode materials, but this is ascribed to the lower orthorhombic symmetry of its crystal structure.<sup>14,41</sup>

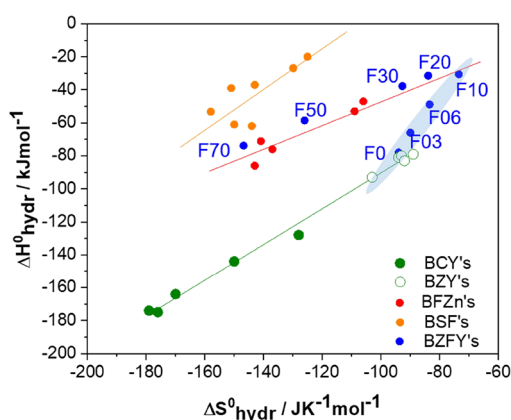


**Figure 2.** Plot of  $\Delta H_{\text{hydr}}^{\circ}$  vs  $\Delta S_{\text{hydr}}^{\circ}$  of various materials:  $(\text{Ba,Sr})\text{FeO}_{3-\delta}$  (BSF),  $\text{Ba}(\text{Fe,Y,Zn})\text{O}_{3-\delta}$  (BFZn),  $\text{Ba}(\text{Zr,Y})\text{O}_{3-\delta}$  (BZY),  $\text{Ba}(\text{Ce,Y})\text{O}_{3-\delta}$  (BCY), and  $\text{Ba}(\text{Zr,Y,Fe})\text{O}_{3-\delta}$  (BZFY, blue points). BCY and BZY data from ref 14, and BSF and BFZn from ref 20. The transition between electrolyte and electrode behaviors is highlighted in the blue shade.

Figure 2 illustrates for the BZFY solid solution how the low-iron compositions (<10 mol %, highlighted by blue shade) smoothly fill the gap between electrolyte and electrode material behaviors.  $\Delta S_{\text{hydr}}^{\circ}$  largely remains in the range of  $-80$  to  $-100 \text{ J mol}^{-1} \text{ K}^{-1}$  typical for  $\text{BaZrO}_3$  electrolytes, but  $\Delta H_{\text{hydr}}^{\circ}$  increases from  $-80$  to  $-31 \text{ kJ mol}^{-1}$  which then results

in less negative  $\Delta G_{\text{hydr}}^{\circ}$ . When more iron is introduced, the materials more and more approach the typical behavior of other cathode materials. From F20 to F70, the hydration enthalpy becomes more negative again (more and more  $\text{Zr}^{4+}$  is replaced by the less charged  $\text{Fe}^{3+}$ ), but in parallel,  $\Delta S_{\text{hydr}}^{\circ}$  also becomes more negative, such that the overall  $\Delta G_{\text{hydr}}^{\circ}$  remains positive at about  $+30 \text{ kJ mol}^{-1}$ .

Density functional theory (DFT) calculations of proton and hydroxide affinity for a large range of oxides showed that materials with a smaller ionization potential exhibit a larger proton affinity and overall have more negative hydration enthalpies.<sup>42</sup> This relation may appear surprising because the hydration reaction (eq 1) is amphoteric as it comprises the protonation of an oxide ion as well as the incorporation of hydroxide into  $\text{V}_{\text{O}}^{\circ}$ . However, the calculations in ref 42 also show that the proton affinity varies more strongly from material to material and outweighs the opposite trend of the hydroxide affinity. Thus, the hydration enthalpy correlates with the proton affinity, which can be regarded as a measure of the basicity in the considered oxides. This is in line with the phenomenological observation that oxides with higher basicities such as electrolyte-type materials often have a more negative  $\Delta H_{\text{hydr}}^{\circ}$ . The effect of local distortions on the basicity of oxide ions is discussed in more detail in Section 3.2. The reason for the more negative  $\Delta S_{\text{hydr}}^{\circ}$  in electrode materials compared to electrolytes requires a detailed analysis of the phonons, which are sensitive to local and overall symmetry

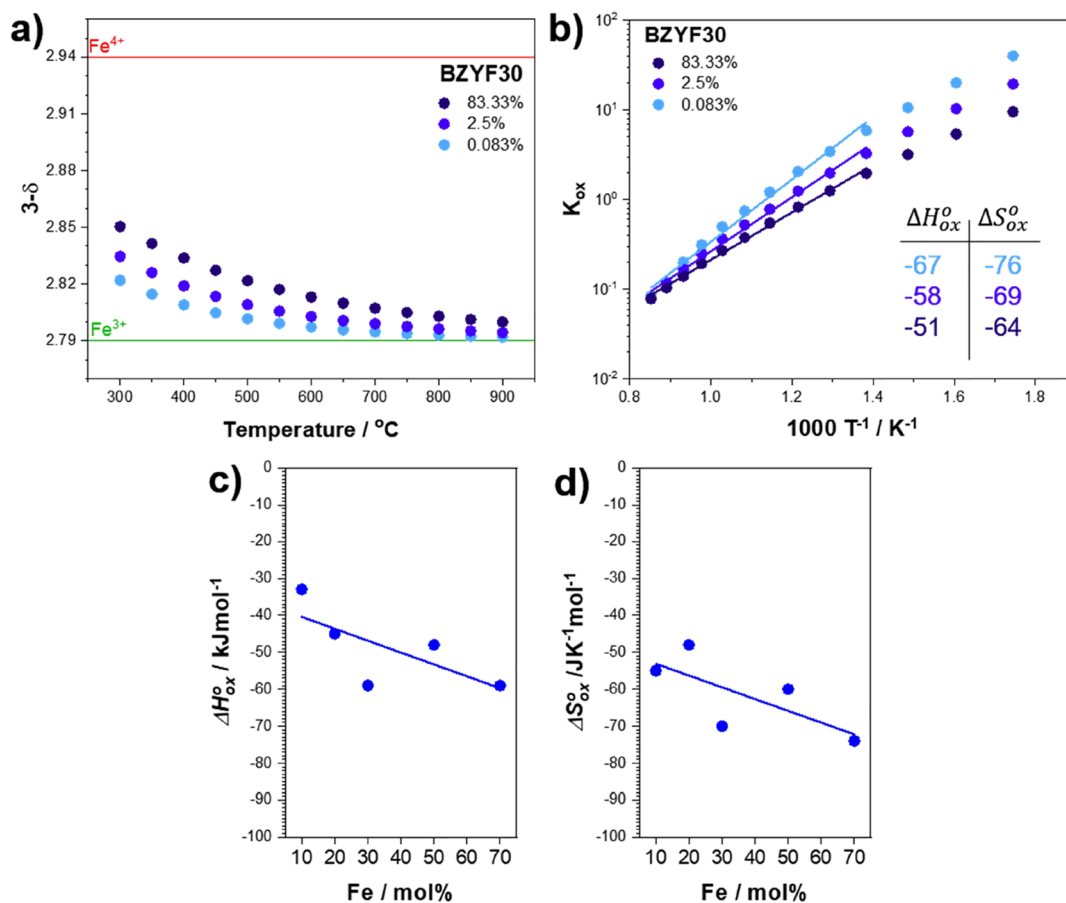


**Figure 3.** (a, b) Exemplary oxygen stoichiometry  $3 - \delta$  and Van't Hoff plots for F30. The indicated borders for complete  $\text{Fe}^{3+}$  and  $\text{Fe}^{4+}$  formation are calculated from the electroneutrality condition. The  $\Delta H_{\text{ox}}^{\circ}$  and  $\Delta S_{\text{ox}}^{\circ}$  values are reported for each  $p\text{O}_2$ . (c, d) Standard enthalpy and entropy of oxidation as a function of Fe content (taking the average over all  $p\text{O}_2$ ).

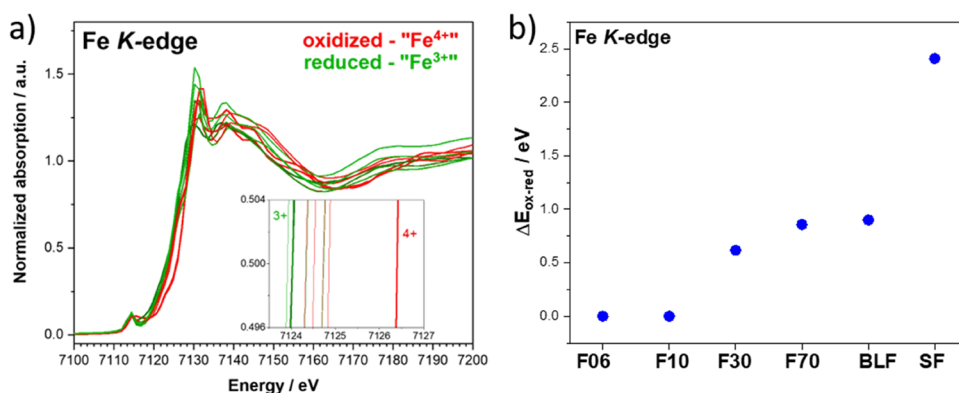


**Figure 4.** (a) Fe K-edge XANES of all BZFY samples (Figure S9 shows the separate spectra).  $\text{SrFeO}_{3-\delta}$  standards are reported as bold lines. Oxidized and reduced samples are reported in red and green, respectively. The inset magnifies the half-height of the edge. (b) Difference of edge position (at half-height) between oxidized and reduced samples as a function of material composition. BLF data are from ref 34.

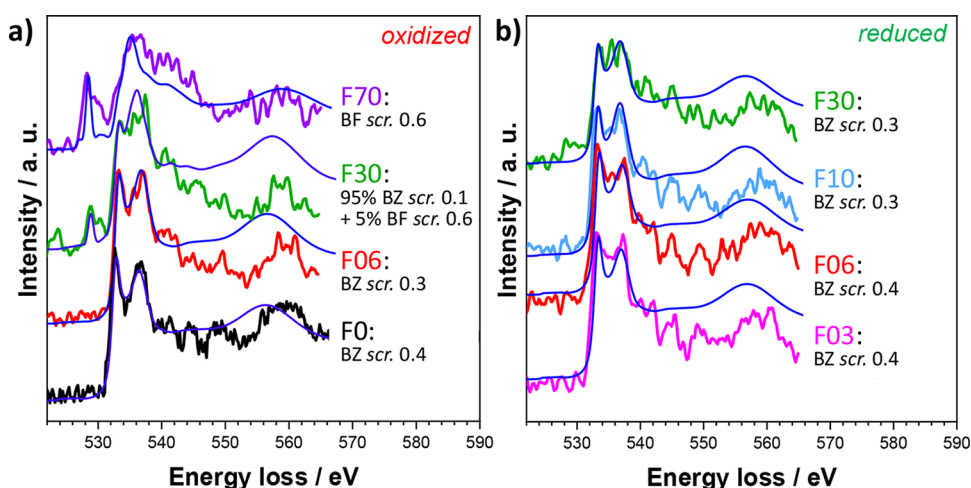


**Figure 5.** O K-edge spectra of (a) oxidized and (b) reduced BZYF samples. The appearance of a pre-edge in (a) indicates the intermixing of the  $\text{O}2p\text{-Fe}3d$  orbitals. The best spectra simulations are overlaid as dark blue lines; the starting structure used in the simulation (BF=  $\text{BaFeO}_3$  or BZ=  $\text{BaZrO}_3$ ) and applied screening values are indicated. For all samples, the value of the *dilatorb* parameter is 0.1.

reduction, and their changes upon hydration. This is currently under investigation but beyond the scope of the present publication.

The trends in hydration thermodynamics observed here for substitution of increasing amounts of Fe into  $\text{Ba}(\text{Zr},\text{Y})\text{O}_{3-z}$  are expected to hold also for related materials such as barium cerate electrolytes and also for substitution with neighboring redox-active transition metals (Co, Ni) as they also form highly covalent TM–O bonds.

**3.1.2. Oxygen Stoichiometry.** Figure 3a,b reports an exemplary oxygen stoichiometry plot for F30 (other samples reported in Figure S8). Most van't Hoff plots depart from linearity, in particular at low T and high  $p\text{O}_2$ , indicating a deviation from ideal dilute behavior. Such nonidealities have been observed for  $K_{\text{ox}}$  of other redox-active perovskites and have been attributed to hole–hole interactions.<sup>43,44</sup>

The hole–hole interaction is attributed to the fact that holes are not strictly localized on the transition metal but are more or less delocalized to adjacent oxygen ions and correspondingly has a larger range of influence.<sup>22</sup> The partial hole transfer to O is also supported by DFT calculations for  $\text{BaFeO}_3$  showing that the states beneath the Fermi level have predominant O character.<sup>25,45</sup> When hole–hole interactions are perceptible in oxygen stoichiometry measurements, the corresponding hole

transfer to O is expected to affect also the hydration behavior, that is, to decrease the proton uptake. This trend is indeed seen in the present samples such as F20 and F30 which show strongest nonidealities in  $K_{\text{ox}}$  and in parallel a comparably low proton uptake.

The trend of  $\Delta H_{\text{ox}}^\circ$  and  $\Delta S_{\text{ox}}^\circ$  with Fe content is depicted in Figure 3c,d. The oxidation enthalpy becomes more negative with an increase in the iron amount. This can be related to the decreasing lattice parameter, which makes the size of the  $\text{BO}_6$  octahedron more suitable for the presence of (formal)  $\text{Fe}^{4+}$  ions and/or oxide ions with partial hole transfer, which are smaller than  $\text{Fe}^{3+}$  and/or  $\text{O}^{2-}$  ions without transferred holes.

**3.2. X-ray Spectroscopy.** **3.2.1. Iron XANES.** The Fe K-edge XANES spectrum gives information about the average coordination and effective oxidation state of iron. Figure 4a shows the spectra for all of the measured compositions. The edge positions of all BZFY samples are located in the rather narrow range of 7124.0–7124.8 eV. For comparison, we also include  $\text{SrFeO}_{2.5}$  and  $\text{SrFeO}_3$ . Also,  $\text{SrFeO}_3$  may partially have hole transfer to O (“ligand hole” instead of complete  $\text{Fe}^{4+}$ ). However, the fact that  $\text{SrFeO}_3$  shows the largest edge shift between reduced and oxidized samples (oxidized  $\text{SrFeO}_3$  at significantly higher energy of 7126.5 eV) indicates that  $\text{SrFeO}_3$  has much less ligand hole character than  $\text{BaFeO}_3$ , that is, iron

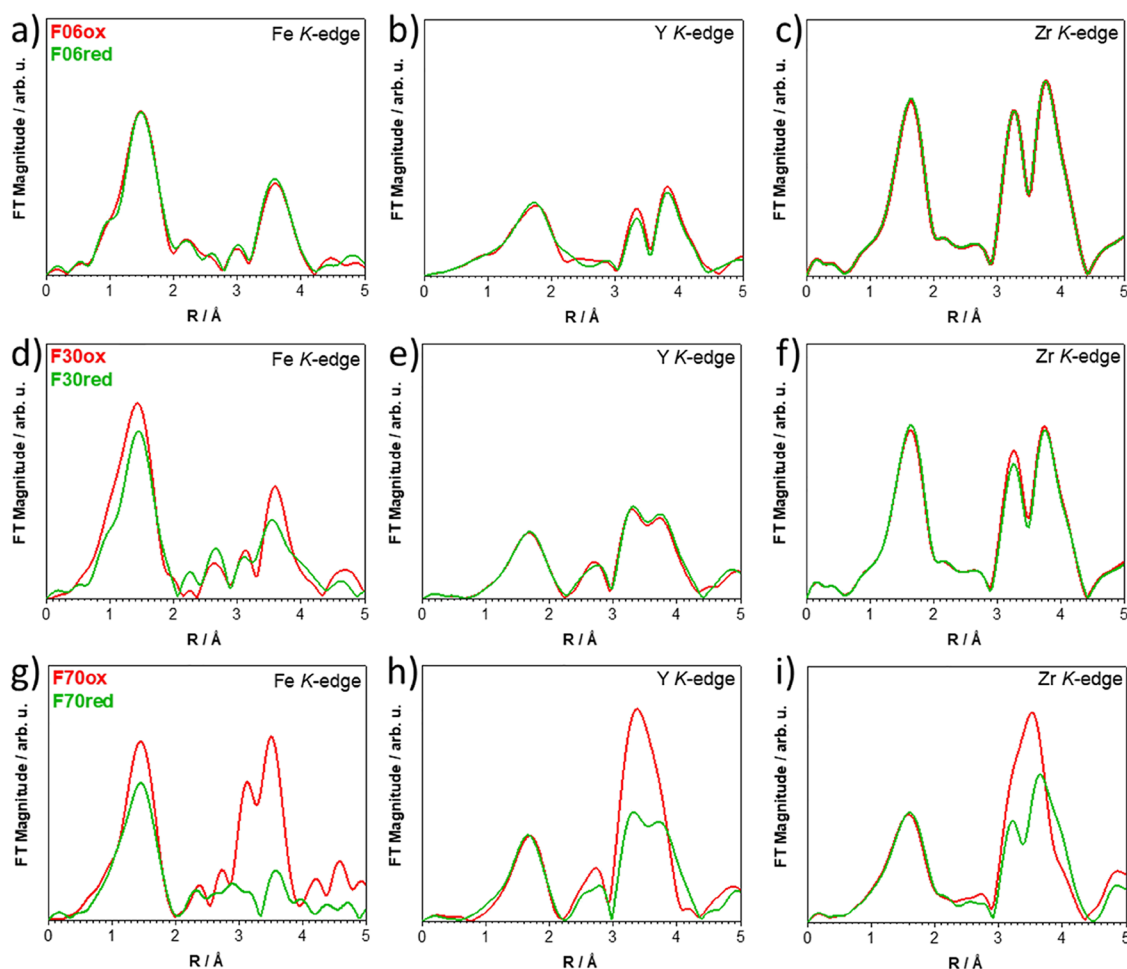


**Figure 6.** Fourier transforms of oxidized and reduced F06 (a–c), F30 (d–f), and F70 (g–i) at the Fe, Zr, and Y K-edges. The corresponding plot for F10 can be found in Figure S17.

is closer to  $\text{Fe}^{4+}$ . The comparably high edge energy for  $\text{SrFeO}_3$  has been explained in ref 34 as stemming from the lower overall basicity of  $\text{SrFeO}_3$ ; therefore, the ability of O to accept holes is also smaller than for  $\text{BaFeO}_3$ .

For the BZFY samples, the similarity of the edge position between the reduced and oxidized samples (Figure 4b, Table S4) indicates that the effective Fe valence of the latter is still rather close to that of the reduced materials. The lower effective oxidation state is attributed to the partial electron hole transfer from  $\text{Fe}^{4+}$  to the adjacent oxide ion<sup>26,35,46,47</sup> that is confirmed also in the O K-edge spectra discussed below. As demonstrated in refs 34,35, this effect decreases the basicity of the oxide ion, hindering the hydration.

In Figure 4b, the edge shift between oxidized and reduced BZFY samples is larger for F30, F70, and BLF (but still much less than for  $\text{SrFeO}_3$ ) compared to the compositions with a low Fe content. This might be related to the fact that iron-poor materials still exhibit the large lattice parameter of  $\text{BaZr}_{0.88}\text{Y}_{0.12}\text{O}_{2.94}$ , which favors Fe cations in the lower oxidation state. The fact that the effective Fe oxidation state in oxidized F30 and F70 is higher than in F06 and F10 is not in contradiction with the slightly increasing degree of hydration in Figure 1b. The hole delocalization to O is just one of several effects influencing hydration; also lattice parameter, symmetry lowering and energetically inequivalent protonation sites, cation radii mismatch, basicity of dopants, and so forth may

all affect hydration.<sup>20,35</sup> Finally, it is important to note that the proton uptake is measured on samples quenched from 700 °C in  $\text{N}_2$  to preserve a high  $[\text{V}_\text{O}]$  (all iron formally  $\text{Fe}^{3+}$ ), that is, the hole concentration is negligible under these conditions.

**3.2.2. Oxygen X-ray Raman scattering.** The K-edge spectra of reduced and oxidized samples measured in the X-ray Raman scattering (XRS) mode are reported in Figure 5. As expected, for a low Fe content, the spectrum of oxidized F06 is quite similar to that of the undoped  $\text{BaZrO}_3$  reference (F0). For low Fe content F03–F10, the spectra of the reduced samples are also very similar to those of the oxidized F06; only the splitting between the peaks at  $\approx 533$  and  $\approx 538$  eV is slightly less pronounced. These peaks are assigned to  $(\text{Zr}/\text{Y})d$  orbitals intermixed with the  $\text{O}_{sp}$  (533 eV) and hybridized orbitals with mainly the  $\text{O}_{p\text{-TMD}}$  character (538 eV). This assignment is based on the projected density of states reported in Figure S11. For F30, significant differences appear between the reduced and oxidized samples and also to lower-Fe materials. In reduced F30, the intensity ratio of the double peak is modified such that the components at 533 and 538 eV appear with comparable intensity. For oxidized F30, a pre-edge feature at  $\approx 527$  eV develops, which is assigned to  $\text{Fe}3d\text{-O}2p$  hybridized orbitals and characteristic for the presence of holes in O states. These changes become even more pronounced for oxidized F70, where the pre-edge peak is very prominent, and the component at 533 eV has almost completely vanished. This

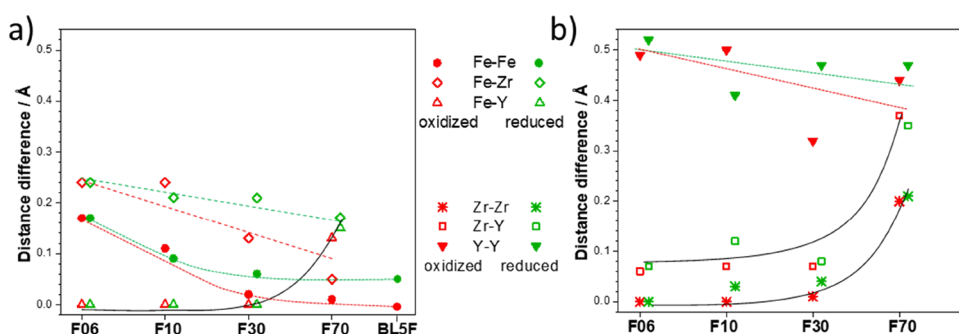


**Figure 7.** Difference between 2 M–O and M–M (a) for paths involving iron atoms, including BLSF data from ref 34, and (b) for paths involving Zr with Zr,Y as well as Y,Y (the typical uncertainty of these values is  $\pm 0.12$  Å). A larger difference means stronger buckling of the respective configuration; the lines serve as a guide to the eye. The Fe–Fe difference for F70red is missing because of the low 3rd shell signal at the Fe *K*-edge (cf. Figure S19d).

spectrum is rather similar to the ones reported in ref 35 for other Zn and Y-doped barium ferrates.

We simulated the O *K*-edge spectra with the same methodology used in ref 35 applying two semiempirical parameters *screening* and *dilatorb* to account for dopant effects on the interaction between TMs *d* and O *2p* orbitals and for eventually increased orbital overlap. The effect of applying different *screening* values is illustrated in Figure S12, and it strongly changes the intensity ratio of the 533 and 538 eV components. The simulated spectra are superimposed in Figure 5 as dark blue lines. BaZrO<sub>3</sub> (F0) is used as reference for both oxidized and reduced samples, and it can be simulated with a good match to experimental data with a *screening* value of 0.4 and *dilatorb* of 0.1 (*dilatorb* = 0.1 is the appropriate value for all spectra). For the oxidized samples, the *screening* values decrease with increasing iron content from F0 to F30, indicating a gradual increase in covalency. This is also supported by the appearance of the pre-edge peak. The absence of the pre-edge in F06ox is most probably due to the too low iron content, but the fact that a lower *screening* value than that for F0 has to be applied indicates increased covalency in the system. The increased covalency of Fe–O bonds will also affect the electronic conductivity, as discussed in Section 3.3. The reduced samples (Figure 5b) can be simulated using the same *screening* values as obtained for F0 for F03 and F06, while *screening* = 0.3 is used for F10 and F30. The higher *screening* values applied to simulate the reduced samples compared to their oxidized counterparts confirm the lower covalency in these samples, as expected for materials containing iron only in the formal 3+ oxidation state.

**3.2.3. EXAFS.** The Fourier-transformed EXAFS data of all samples are shown in Figure 6, while detailed fittings and results are reported in the Supporting Information (Tables S5–6 and Figures S13–19). The most important structural effects are however clearly visible already in the raw experimental data: in F06 (i.e., when iron acts as a dopant in Ba(Zr,Y)O<sub>3-z</sub>), structural changes between oxidized and reduced are minimal on all edges. At intermediate composition (F30), the iron local environment shows larger variation with [V<sub>O</sub>] (i.e., between oxidized and reduced state) than the Y and Zr edges. For F30 and F70, the first-shell Fe–O peak is lower for reduced compared to oxidized samples, consistent with a decrease in the Fe–O coordination number. This effect is more evident at higher Fe content, while Y–O and Zr–O remain unperturbed; this implies a clustering of the oxygen vacancies around iron, as concluded also in ref 35 for doped

BaFeO<sub>3-δ</sub>. At a high Fe content (F70), drastic changes due to the high V<sub>O</sub> content affect the whole lattice, also influencing Zr–M and Y–M third-shell distances. In particular, the lower intensity around 3–4 Å is fitted with the appearance buckling in the Fe–O–Fe as well as Fe–O–(Zr,Y) and (Zr,Y)–O–(Zr,Y) connections (similar features are observed for differently doped BaFeO<sub>3-δ</sub> in ref 34).

The buckling of M–O–M connections (i.e., local octahedra tilting) is quantified from the difference of the direct M–M distance to the sum of the two M–O distances; for a perfectly linear M–O–M arrangement, this difference vanishes. Non-zero values imply M–O–M buckling, which leads to a lower intensity of the third shell peak. A M–O–M buckling angle <180° has been correlated with increased oxygen ion basicity caused by the decreased TM3d–O2p hybridization in several publications.<sup>22,34,35</sup> In Figure 7, we follow the same approach as in ref 34, but the picture is much more complex, given the simultaneous presence of three different B-site cations. Nevertheless, some trends can still clearly be identified. For the Fe–O–M arrangements, Figure 7a shows that increasing iron content decreases buckling of the Fe–O–Fe bonds and, to a smaller degree also, of Fe–O–Zr bonds for both oxidized and reduced samples. The decrease of Fe–O–Fe buckling by increasing the iron content can be explained from the fact that Fe is the native element in a BaFeO<sub>3-δ</sub> matrix (cf. BLSF data<sup>34</sup>), while for low-Fe materials, it is an undersized dopant in the BaZr<sub>0.88</sub>Y<sub>0.12</sub>O<sub>2.94</sub> matrix. The decreased Fe–O–Fe buckling for increased iron content correlates very well with the higher electronic conductivity; this will be discussed in more detail in Section 3.3.

In contrast to Fe–O–Fe, the buckling of Fe–O–Y increases with increasing iron concentration (similarly for oxidized as well as reduced samples). This can be understood from the fact that the lattice parameter of Fe-rich materials is decreased, which makes Y<sup>3+</sup> an even more oversized dopant. The pronounced Fe–O–Y buckling in Fe-rich compositions is expected to favor the proton uptake (cf. refs 20,22,34). Specifically, F70 (and F80 with similar distortions expected) has a significantly higher proton uptake compared to BLSF (Figure 1) in which such Fe–O–Y buckling is absent. Also, Y–O–Y connections involving two oversized dopants are strongly buckled for all Fe contents (Figure 7b). Opposite to Fe–O–Fe, the distortion in the Zr–O–Zr and Zr–O–Y bonds increases for high iron content since in a BaFeO<sub>3-δ</sub> matrix, both Zr<sup>4+</sup> and Y<sup>3+</sup> are oversized dopants (Figure 7b).

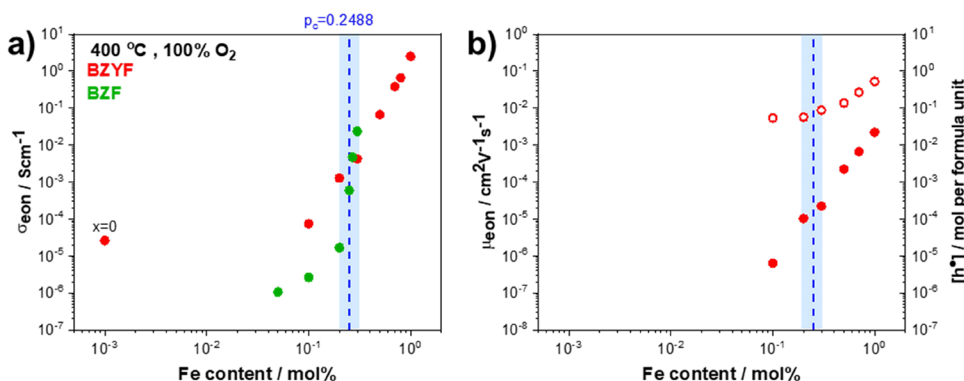


**Figure 8.** (a) Electronic conductivity  $\sigma_{\text{eon}}$  of BZYF and BZF ( $\text{BaZr}_{1-x}\text{Fe}_x\text{O}_{3-\delta}$  from ref 27). (b) Hole mobility  $\mu_{\text{eon}}$  (solid symbols) and concentration  $[\text{h}^+]$  (open symbols) as a function of iron content in BZYF. The blue shade indicates the critical percolation region. Data for  $x = 0$  taken from ref 49.

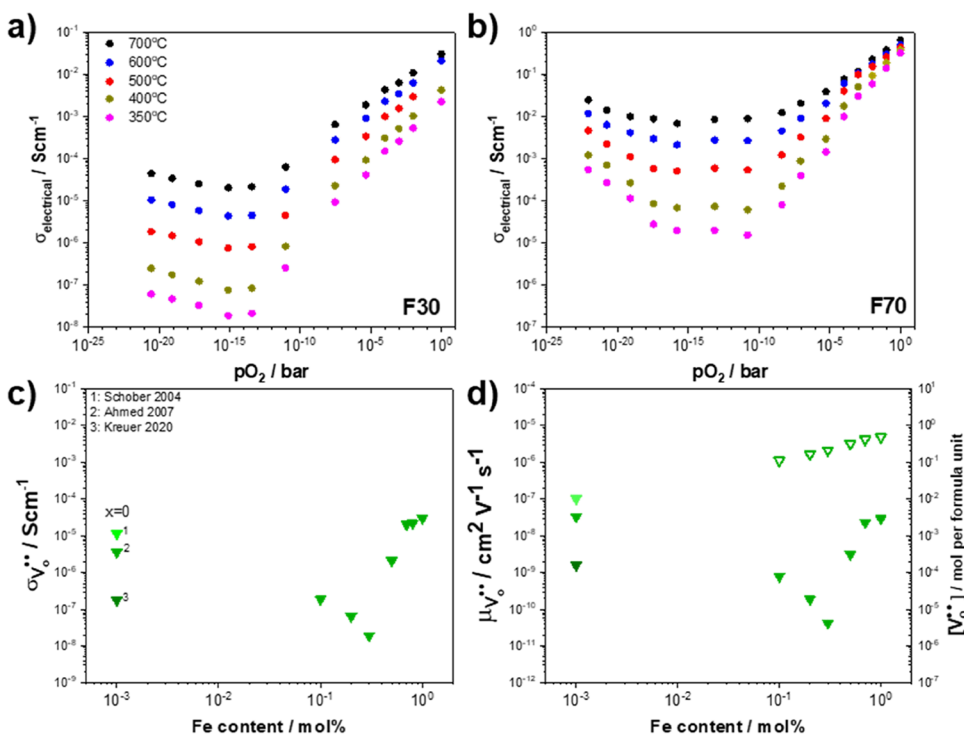


**Figure 9.** Conductivity in dry atmosphere of (a) F30 and (b) F70 as a function of  $p\text{O}_2$ . (c) Oxygen vacancies conductivity and (d)  $V_{\text{O}}^{\bullet}$  mobilities and concentrations at 350 °C as a function of iron content. The data for  $x = 0$  refer to  $\text{BaZr}_{0.9}\text{Y}_{0.1}\text{O}_{2.95}$  and  $\text{BaZr}_{0.9}\text{Yb}_{0.1}\text{O}_{2.95}$ , taken from refs 61–63.

As a very rough measure of overall distortion, one can add the contributions from the individual atom pairs. For the reduced samples (which correspond to the TG measurement conditions), this yields the largest total distance difference (1.35 Å) for F70 compared to F30 and F10 (0.86 Å) and F06 (1.00 Å). This agrees nicely with the trend in hydration (Figure 2) that F10–F30 samples exhibit the minimum of proton uptake and degree of hydration and indicates that the large amount of local distortions is one of the key parameters for the comparably high proton uptake of F70.

**3.3. Electrical Conductivity.** **3.3.1. Electronic Conductivity in Dry 100%  $\text{O}_2$ .** The p-type electronic conductivity at 400 °C is reported as a function of iron content in Figure 8. From the oxygen stoichiometry and electroneutrality condition, the total hole concentration is calculated taking  $[\text{h}^+] = [\text{Fe}^{4+}] = 1 - 2[V_{\text{O}}^{\bullet}]$ . The obtained effective hole mobility (Figure 8b) is mainly responsible for the increase in

$\sigma_{\text{eon}}$ , and the relative changes of hole concentration are smaller. Figure 8a shows a sharp rise in electronic conductivity by more than 5 orders of magnitude. The proximity of this increase to the nominal percolation threshold (critical concentration  $p_c = 0.2488$  for an ideal cubic model<sup>48</sup>) might suggest a percolation-type phenomenon for the electronic transport. Such an attribution should be regarded with some caution; in ref 27, the term *percolation region* is used. In fact the increase starts just above a Fe fraction of 0.1, and several effects are expected to influence such an increase of  $\sigma_{\text{eon}}$ , for example, the degree of localization/delocalization of the carrier and the distribution of counter charges relative to dopants. In the present materials, holes strongly interact with Fe. For low Fe content, a detrapping from these centers is required for long-range transport. This can be avoided for sufficiently close Fe neighbors, leading to a percolation-type  $\sigma_{\text{eon}}$  increase with the Fe content.

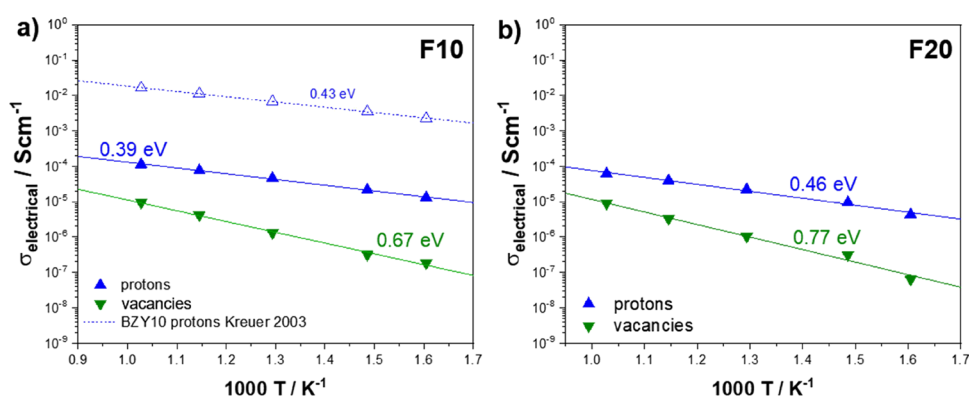


**Figure 10.** Bulk ionic conductivities of (a) F10 and (b) F20; blue = proton conductivity, green = oxygen vacancy conductivity. Data of hydrated  $\text{BaZr}_{0.9}\text{Y}_{0.1}\text{O}_{3-z}$ <sup>14</sup> serve as reference for proton conductivity in an electrolyte.

It is well-known that for barium ferrates, the *p*-type conductivity occurs via small polaron hopping along the TM–O network.<sup>39,50–53</sup> Thus, a correlation of the conductivity with variation of the iron concentration is highly expected. In the simplest model, the presence of oxygen vacancies is neglected, which interrupt the conduction network and thus also act as an obstacle (see e.g., hole mobility as a function of  $[\text{V}_{\text{O}}^{\bullet}]$  for  $\text{SrFeO}_{3-\delta}$ <sup>51</sup> and  $(\text{La,Sr})\text{FeO}_{3-\delta}$ <sup>50</sup>). Also M–O–M buckling will decrease the hole mobility.<sup>54–56</sup> The present samples are measured in a dry oxidizing atmosphere where  $[\text{V}_{\text{O}}^{\bullet}]$  is moderate (Figure S8), but on a qualitative level, the data are described reasonably well.

In the simplest approximation, three types of transfers are possible for the holes. For low iron content, the isolated Fe acts as trapping centers, that is, the holes need to be detrapped before they can migrate over longer distances along  $\text{ZrO}_6$  octahedra (the detrapping energy is estimated to 0.8–1.2 eV for  $\text{BaZr}_{1-x}\text{Fe}_x\text{O}_{3-\delta}$ ,<sup>27,57</sup> cf. also  $\approx 1.2$  eV for  $\text{SrTi}_{1-x}\text{Fe}_x\text{O}_{3-\delta}$ <sup>58</sup>). For intermediate iron concentrations, hole hopping occurs through a framework of mixed  $\text{ZrO}_6$  and  $\text{FeO}_6$  octahedra, where some trapping effects are still present. For iron amounts exceeding the percolation region, the holes move largely through connected  $\text{FeO}_6$  octahedra (free of trapping events), and correspondingly the hole mobility increases steeply as shown in Figure 8b. The fact that the increase occurs already directly above an Fe fraction of 0.1 indicates that facile hole transfer is not strictly limited to direct Fe–O–Fe contacts. This is in line with the larger range of influence that the hole acquires by being partially delocalized from the Fe to O states. DFT calculations find that the band gap is close to vanishing for  $x = 0.125$  when Fe in  $\text{BaZr}_{1-x}\text{Fe}_x\text{O}_3$  is arranged such that linear Fe–O–Zr–O–Fe paths exist.<sup>57</sup>

For comparison, Figure 8a also shows the change of electronic conductivity in the  $\text{BaZr}_{1-x}\text{Fe}_x\text{O}_{3-\delta}$  solid solution without Y addition (data from ref 27). There are two characteristic differences: (i) for low Fe and thus low  $\text{V}_{\text{O}}^{\bullet}$  concentration, the conductivity is lower than for BZYF. This can be attributed to the fact that the increased  $[\text{V}_{\text{O}}^{\bullet}]$  upon  $\text{Y}^{3+}$  doping leads to an increased hole concentration from the oxygenation reaction of eq 2, cf. the hole formation in  $\text{BaZr}_{1-x}\text{Y}_x\text{O}_{3-z}$ .<sup>59</sup> (ii) The conductivity increase around  $p_c$  is less steep in BZYF than in BZF. This is most probably related to a higher amount of local distortions in BZYF related to the oversized  $\text{Y}^{3+}$  dopants. A comparable increase of electronic

conductivity with transition metal content is also found for the  $\text{BaZr}_{1-x}\text{Co}_x\text{O}_{3-\delta}$  solid solution.<sup>60</sup>

**3.3.2. Electrical Conductivity Using the Oxygen Pump.** Figure 9a,b reports the conductivities in dry condition as a function of  $p\text{O}_2$  for F30 and F70, and other sample compositions are shown in Figure S22. In accordance with the expected Brouwer diagrams,<sup>64</sup> one recognizes three different regimes of  $p\text{O}_2$  dependence. Electron holes are the dominant charge carriers for  $1 < p\text{O}_2 < 10^{-5}$  bar, conduction electrons for  $p\text{O}_2$  lower than approximately  $10^{-18}$  bar (the *n*-type branch is only slightly visible in F30, more pronounced for F70). In the intermediate  $p\text{O}_2$  range, the conductivity is approximately independent of  $p\text{O}_2$  and can be attributed to oxygen vacancies. Figure 9c summarizes the  $\text{V}_{\text{O}}^{\bullet}$  conductivities as a function of iron content. Starting from literature data for Fe-free materials (which exhibit some scatter), the values decrease upon introducing iron up to F30 and then increase again. Figure 9d demonstrates that this variation mainly originates from the change in effective  $\text{V}_{\text{O}}^{\bullet}$  mobility.

For low iron content, the decrease in mobility can be attributed to trapping of  $\text{V}_{\text{O}}^{\bullet}$  close to iron cations, in agreement with the EXAFS results that indicate a preferred location of  $\text{V}_{\text{O}}^{\bullet}$  at Fe. As long as the trapping regions do not form an overlapping path, an increased concentration of trap centers decreases the effective mobility. For higher iron contents, clustering of  $\text{V}_{\text{O}}^{\bullet}$  around Fe still prevails, but for more than 30 mol % iron, the trapping regions can form a path for  $\text{V}_{\text{O}}^{\bullet}$  migration without the need of detrapping (this may be regarded as a percolation effect for ionic carriers). Correspondingly, the effective  $\text{V}_{\text{O}}^{\bullet}$  mobility increases. The  $\text{V}_{\text{O}}^{\bullet}$  migration activation energies are summarized in Figure S23.

In addition, the Fe–O bond covalency may also play a role. As discussed in Sections 3.2 and 3.3, with increasing Fe content more Fe3*d*–O2*p* orbital hybridization is present, which could decrease the effective ion radius of O (transfer of electron density from O to Fe, to some degree expected even for reduced samples). Such a decreased oxide ion radius would facilitate the oxygen ion migration, cf. the concept of passing through the “critical triangle” of the B-site and two A-site cations.<sup>65</sup> On the other hand, the decreasing lattice parameter for Fe-rich materials would narrow the available space for the oxide ion jump. However, the discussion of  $\text{V}_{\text{O}}^{\bullet}$  mobilities for various perovskites in ref 66 shows the highest mobilities in materials with high B–O bond covalency such as titanates and redox-active perovskites. DFT calculations for oxide ion migration in  $\text{Ba}_{1-x}\text{Sr}_x\text{Co}_{1-y}\text{Fe}_y\text{O}_{3-\delta}$  perovskites demonstrated

that transient electron transfer from O to a highly redox-active B-cation in the transition state further lowers the migration barrier.<sup>67</sup>

Measurements in the oxygen pump can also be conducted in a humidified atmosphere. For F10 and F20, this yields a higher conductivity than in dry conditions (Figures 10 and S22), the difference being caused by the appearance of proton conductivity. This approach works well as long as the difference is sufficiently large, but for Fe-rich materials, the difference vanishes. The activation energies for proton conductivity in F10 and F20 are comparable to that of the  $\text{BaZr}_{0.9}\text{Y}_{0.1}\text{O}_{3-z}$  electrolyte, but the absolute values of proton conductivity are significantly lower, owing to the decreased proton concentration.

**3.4. Combined Discussion.** The proton uptake of perovskite materials depends on several factors such as  $V_{\text{O}}$  concentration and geometric as well as the electronic structure, which are investigated here along the  $\text{BaZr}_{0.88-x}\text{Y}_{0.12}\text{Fe}_x\text{O}_{3-\delta}$  solid solution series. This combined discussion now summarizes the most important relations. The hydration measurements show a steep decrease of proton uptake already for low Fe content. The transition from a well-hydrating electrolyte-type material to a low-hydrating mixed conductor is largely completed already for 10 mol % Fe, as evidenced by the changes in  $\Delta H_{\text{hydr}}^{\circ}$  and  $\Delta S_{\text{hydr}}^{\circ}$ . This transition is not directly determined by a threshold of electronic transference number but rather related to the modification of the properties of the oxide ions. Fe XANES and O XRS measurements indicate a strong covalency on the Fe–O bonds, which decreases the basicity of the oxide ions and thus also the favorability of the hydration reaction. Since one Fe affects six adjacent and maybe even more distant oxygens, a low Fe concentration already has a strong effect on the overall proton uptake. The hydration thermodynamics is highly sensitive to the electronic structure of the oxygen ions,<sup>22</sup> as expressed for example by the ionization potential.

For  $\text{BaZr}_{0.88-x}\text{Y}_{0.12}\text{Fe}_x\text{O}_{3-\delta}$  samples containing more than 30 mol % of iron, the proton concentration increases again to some degree driven by the increased  $V_{\text{O}}$  concentration. Also,  $\Delta H_{\text{hydr}}^{\circ}$  becomes more negative which can be attributed to the replacement of  $\text{Zr}^{4+}$  with  $\text{Fe}^{3+}$  and the increased M–O–M buckling as evidenced by the EXAFS results. The importance of the buckling which helps to preserve a high basicity of the oxide ions is also clearly demonstrated by the comparison of the proton uptake of F70 and F80 (4.1–4.2%, Figure 1) which is more than twice higher than that of BLSF (1.8%) with only minor buckling (Figure 7a). For perovskites, it is well-known that the extent of  $\text{O}2p\text{-TM}3d$  orbital interaction decreases strongly when the TM–O–TM connection deviates from linearity (e.g. refs 68–70), and thus also the amount of hole transfer from the Fe to O. Oxygen *K*-edge spectra of Zr,Y,Zn doped barium ferrates in Figure 5a and refs 34,35 show a modified shape of the pre-edge features compared to BLSF which also indicates a decreased hole transfer to O. This explains the pronounced effect of dopant-induced local distortions on the hydration.

The *p*-type electronic conductivity in oxidizing conditions increases steeply above 10 mol % Fe. The partial hole delocalization from Fe to O, as evidenced in particular by O XRS, increases the holes' range of influence and broadens the percolation-type transition of  $\sigma_{\text{con}}$ . However, only for high Fe content >70 mol %, the absolute values of  $\sigma_{\text{con}}$  reach a magnitude acceptable for an electrode material ( $\geq 1$  S/cm).

The ionic conductivity from  $V_{\text{O}}$  shows a moderate decrease from low to intermediate Fe contents, which is attributed to trapping of  $V_{\text{O}}$  at still separated Fe centers (this is supported by the EXAFS results). For Fe contents >30 mol %, the  $V_{\text{O}}$  conductivity increases as a consequence of two effects. At higher Fe content, the trapping zones begin to overlap, and  $V_{\text{O}}$  can migrate without need for detrapping. Furthermore, the increasing Fe–O covalency is expected to lower the  $V_{\text{O}}$  migration barriers.

Unfortunately, with the methods applied here, the proton conductivity could not be resolved for Fe-rich samples. While systematic investigations of proton mobilities in triple-conducting perovskites are not available yet, estimations from chemical diffusion experiments indicate that it is not drastically lower than that in  $\text{Ba}(\text{Zr},\text{Y})\text{O}_{3-z}$  electrolytes.<sup>19</sup> Thus, as a first approximation, we assume that the proton conductivity of Fe-rich materials roughly follows the trend of proton concentration.

A synopsis of the relevant materials' properties in the  $\text{BaZr}_{0.88-x}\text{Y}_{0.12}\text{Fe}_x\text{O}_{3-\delta}$  solid solution series is shown in Figure 11. It illustrates that—instead of combining the advantages of

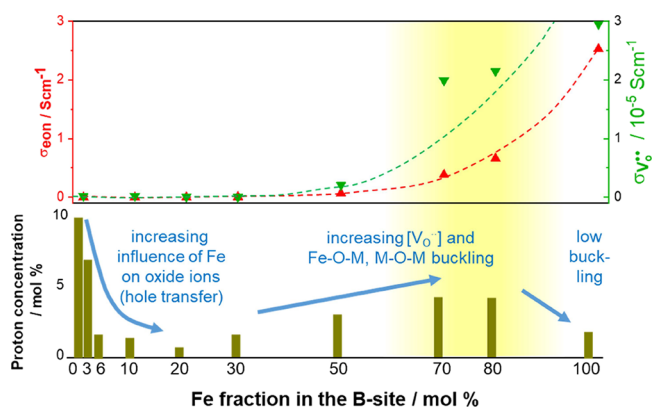


**Figure 11.** Summary of proton uptake and electronic and oxygen ion conductivities as a function of iron content (conditions as in Figures 1, 8, and 9c). The yellow shade highlights the region where a good oxygen electrode material should be located.

electrolyte-type and redox-active perovskites—the materials at low to intermediate Fe contents of 6–30 mol % rather suffer from the simultaneous presence of already decreased proton concentration while not yet developing good electronic conductivity. A good compromise is found for  $\text{BaZr}_{0.88-x}\text{Y}_{0.12}\text{Fe}_x\text{O}_{3-\delta}$  with high Fe content, where the presence of a high  $V_{\text{O}}$  concentration and distortions caused by the oversized Y dopant ensure a still acceptable proton concentration. A similar behavior is expected for other perovskite solid solution series with a gradually increasing redox-active transition metal content in an electrolyte-type host.

## 4. CONCLUSIONS

Materials from the  $\text{BaZr}_{0.88-x}\text{Y}_{0.12}\text{Fe}_x\text{O}_{3-\delta}$  solid solution series ranging from electrolyte-type Fe-poor compositions to Fe-rich electrode-type materials were comprehensively investigated. Proton uptake and electronic conductivity exhibit opposite trends with the iron content. The insights obtained from XAS relate the decrease of proton uptake to the high degree of Fe–O covalency, which decreases the basicity of the oxide ions. Local lattice distortions evidenced by EXAFS spectroscopy

copy decrease O to Fe electron transfer which favors protonation but also lowers the increase of  $\sigma_{\text{con}}$  with increasing Fe content. As a consequence of the counteracting trends, Fe-poor  $\text{BaZr}_{0.88-x}\text{Y}_{0.12}\text{Fe}_x\text{O}_{3-\delta}$  materials do not present a feasible combination of transport properties for the electrode materials in protonic ceramic cells. Rather, Fe-rich members with ca. 20 mol % substitution on the Fe site by redox-inactive oversized dopants are recommended. Furthermore, substitution with moderate amounts of Co or other late transition metals might be favorable in view of an expected higher electronic conductivity and catalytic activity.

## ■ ASSOCIATED CONTENT

### SI Supporting Information

The Supporting Information is available free of charge at <https://pubs.acs.org/doi/10.1021/acs.chemmater.3c01538>.

XRD, UV-vis, TG water uptake and oxygen stoichiometry, additional data for XAS and EXAFS fitting, and conductivity measurement in an oxygen pump (PDF)

## ■ AUTHOR INFORMATION

### Corresponding Authors

**Rotraut Merkle** – Max Planck Institute for Solid State Research, 70569 Stuttgart, Germany; [orcid.org/0000-0003-3811-8963](https://orcid.org/0000-0003-3811-8963); Email: [r.merkle@fkf.mpg.de](mailto:r.merkle@fkf.mpg.de)

**Alessandro Longo** – European Synchrotron Radiation Facility, 38000 Grenoble, France; Istituto per lo Studio dei Materiali Nanostrutturati (ISMN)-CNR, 90123 Palermo, Italy; [orcid.org/0000-0002-8819-2128](https://orcid.org/0000-0002-8819-2128); Email: [alessandro.longo@esrf.fr](mailto:alessandro.longo@esrf.fr)

**Francesco Giannici** – Dipartimento di Fisica e Chimica, Università degli Studi di Palermo, 90123 Palermo, Italy; [orcid.org/0000-0003-3086-956X](https://orcid.org/0000-0003-3086-956X); Email: [francesco.giannici@unipa.it](mailto:francesco.giannici@unipa.it)

### Authors

**Giulia Raimondi** – Max Planck Institute for Solid State Research, 70569 Stuttgart, Germany; [orcid.org/0000-0002-1425-4242](https://orcid.org/0000-0002-1425-4242)

**Olivier Mathon** – European Synchrotron Radiation Facility, 38000 Grenoble, France

**Christoph J. Sahle** – European Synchrotron Radiation Facility, 38000 Grenoble, France

**Joachim Maier** – Max Planck Institute for Solid State Research, 70569 Stuttgart, Germany; [orcid.org/0000-0003-2274-6068](https://orcid.org/0000-0003-2274-6068)

Complete contact information is available at: <https://pubs.acs.org/doi/10.1021/acs.chemmater.3c01538>

### Funding

Open access funded by Max Planck Society.

### Notes

The authors declare no competing financial interest.

## ■ ACKNOWLEDGMENTS

We thank Helga Hoier for XRD, Barbara Baum for sample cutting, and Max Hoedl and Christian Berger for valuable discussions (all MPI, Stuttgart). We acknowledge the European Synchrotron Radiation Facility (ESRF) for provision of synchrotron radiation facilities (proposal MA-4582). We also

thank Noah Kochmann for preparing some of the samples during his internship at MPI Stuttgart.

## ■ REFERENCES

- (1) Yang, L.; Wang, S.; Blinn, K.; Liu, M.; Liu, Z.; Cheng, Z.; Liu, M. Enhanced Sulfur and Coking Tolerance of a Mixed Ion Conductor for SOFCs:  $\text{BaZr}_{0.1}\text{Ce}_{0.7}\text{Y}_{0.2-x}\text{Yb}_x\text{O}_{3-\delta}$ . *Science* **2009**, *326*, 126–129.
- (2) Duan, C.; Tong, J.; Shang, M.; Nikodemski, S.; Sanders, M.; Ricote, S.; Almansoori, A.; O'Hayre, R. Readily processed protonic ceramic fuel cells with high performance at low temperatures. *Science* **2015**, *349*, 1321–1326.
- (3) Morejudo, S. H.; Zanon, R.; Escolastico, S.; Yuste-Tirados, I.; Malerød-Fjeld, H.; Vestre, P. K.; Coors, W. G.; Martínez, A.; Norby, T.; Serra, J. M.; Kjølseth, C. Direct conversion of methane to aromatics in a catalytic co-ionic membrane reactor. *Science* **2016**, *353*, 563–566.
- (4) Malerød-Fjeld, H.; Clark, D.; Yuste-Tirados, I.; Zanon, R.; Catalan-Martinez, D.; Beeaff, D.; Morejudo, S. H.; Vestre, P. K.; Norby, T.; Haugsrud, R.; Serra, J. M.; Kjølseth, C. Thermo-electrochemical production of compressed hydrogen from methane with near-zero energy loss. *Nat. Energy* **2017**, *2*, 923–931.
- (5) Duan, C.; Kee, R. J.; Zhu, H.; Karakaya, C.; Chen, Y.; Ricote, S.; Jarry, A.; Crumlin, E. J.; Hook, D.; Braun, R.; Sullivan, N. P.; O'Hayre, R. Highly durable, coking and sulfur tolerant, fuel-flexible protonic ceramic fuel cells. *Nature* **2018**, *557*, 217–222.
- (6) Choi, S.; Kucharczyk, C. J.; Liang, Y.; Zhang, X.; Takeuchi, I.; Ji, H.-I.; Haile, S. M. Exceptional power density and stability at intermediate temperatures in protonic ceramic fuel cells. *Nat. Energy* **2018**, *3*, 202–210.
- (7) An, H.; Lee, H.-W.; Kim, B.-K.; Son, J.-W.; Yoon, K. J.; Kim, H.; Shin, D.; Ji, H.-I.; Lee, J.-H. A  $5 \times 5 \text{ cm}^2$  protonic ceramic fuel cell with a power density of  $1.3 \text{ W cm}^{-2}$  at  $600 \text{ }^\circ\text{C}$ . *Nat. Energy* **2018**, *3*, 870–875.
- (8) Choi, S.; Davenport, T. C.; Haile, S. M. Protonic ceramic electrochemical cells for hydrogen production and electricity generation: exceptional reversibility, stability, and demonstrated faradaic efficiency. *Energy Environ. Sci.* **2019**, *12*, 206–215.
- (9) Duan, C.; Kee, R.; Zhu, H.; Sullivan, N.; Zhu, L.; Bian, L.; Jennings, D.; O'Hayre, R. Highly efficient reversible protonic ceramic electrochemical cells for power generation and fuel production. *Nat. Energy* **2019**, *4*, 230–240.
- (10) Vøllestad, E.; Strandbakke, R.; Tarach, M.; Catalan-Martinez, D.; Fontaine, M.-L.; Beeaff, D.; Clark, D. R.; Serra, J. M.; Norby, T. Mixed proton and electron conducting double perovskite anodes for stable and efficient tubular proton ceramic electrolyzers. *Nat. Mater.* **2019**, *18*, 752–759.
- (11) Leonard, K.; Deibert, W.; Ivanova, M. E.; Meulenberg, W. A.; Ishihara, T.; Matsumoto, H. Processing Ceramic Proton Conductor Membranes for Use in Steam Electrolysis. *Membranes* **2020**, *10*, 339.
- (12) Dubois, A.; Ricote, S.; Braun, R. J. Benchmarking the expected stack manufacturing cost of next generation, intermediate-temperature protonic ceramic fuel cells with solid oxide fuel cell technology. *J. Power Sources* **2017**, *369*, 65–77.
- (13) Sitte, W.; Merkle, R., Eds. *High-Temperature Electrolysis From fundamentals to applications*; IOP Publishing: Bristol, UK, 2023.
- (14) Kreuer, K. D. Proton-Conducting Oxides. *Annu. Rev. Mater. Res.* **2003**, *33*, 333–359.
- (15) Duan, C.; Huang, J.; Sullivan, N.; O'Hayre, R. Proton-conducting oxides for energy conversion and storage. *Appl. Phys. Rev.* **2020**, *7*, No. 011314.
- (16) Kasyanova, A. V.; Zvonareva, I. A.; Tarasova, N. A.; Bi, L.; Medvedev, D. A.; Shao, Z. Electrolyte materials for protonic ceramic electrochemical cells: Main limitations and potential solutions. *Mater. Rep. Energy* **2022**, *2*, No. 100158.
- (17) Peng, R.; Wu, T.; Liu, W.; Liu, X.; Meng, G. Cathode processes and materials for solid oxide fuel cells with proton conductors as electrolytes. *J. Mater. Chem.* **2010**, *20*, 6218–6225.
- (18) Grimaud, A.; Mauvy, F.; Bassat, J. M.; Fourcade, S.; Rocheron, L.; Marrony, M.; Grenier, J. C. Hydration Properties and Rate

Determining Steps of the Oxygen Reduction Reaction of Perovskite-Related Oxides as H<sup>+</sup>-SOFC Cathodes. *J. Electrochem. Soc.* **2012**, *159*, B683–693.

(19) Poetzsch, D.; Merkle, R.; Maier, J. Proton conductivity in mixed-conducting BSFZ Perovskite from thermogravimetric relaxation. *Phys. Chem. Chem. Phys.* **2014**, *16*, 16446–16453.

(20) Zohourian, R.; Merkle, R.; Raimondi, G.; Maier, J. Mixed-Conducting Perovskites as Cathode Materials for Protonic Ceramic Fuel Cells: Understanding the Trends in Proton Uptake. *Adv. Funct. Mater.* **2018**, *28*, No. 1801241.

(21) Papac, M.; Stevanovic, V.; Zakutayev, A.; O'Hayre, R. Triple ionic–electronic conducting oxides for next-generation electrochemical devices. *Nat. Mater.* **2021**, *20*, 301–313.

(22) Merkle, R.; Hoedl, M. F.; Raimondi, G.; Zohourian, R.; Maier, J. Oxides with Mixed Protonic and Electronic Conductivity. *Annu. Rev. Mater. Res.* **2021**, *51*, 461–693.

(23) Cao, J.; Ji, Y.; Shao, Z. P. Perovskites for protonic ceramic fuel cells: a review. *Energy Environ. Sci.* **2022**, *15*, 2200–2232.

(24) Wang, Z.; Wang, Y.; Wang, J.; Song, Y.; Robson, M. J.; Seong, A.; Yang, M.; Zhang, Z.; Belotti, A.; Liu, J.; Kim, G.; Lim, J.; Shao, Z.; Ciucci, F. Rational design of perovskite ferrites as high-performance proton-conducting fuel cell cathodes. *Nat. Catal.* **2022**, *5*, 777–787.

(25) Hoedl, M. F.; Gryaznov, D.; Merkle, R.; Kotomin, E. A.; Maier, J. Interdependence of Oxygenation and Hydration in Mixed-Conducting (Ba,Sr)FeO<sub>3-δ</sub> Perovskites Studied by Density Functional Theory. *J. Phys. Chem. C* **2020**, *124*, 11780–77189.

(26) Kim, D. Y.; Miyoshi, S.; Tsuchiya, T.; Yamaguchi, S. Electronic Defect Formation in Fe-Doped BaZrO<sub>3</sub> Studied by X-Ray Absorption Spectroscopy. *Chem. Mater.* **2014**, *26*, 927–934.

(27) Kim, D. Y.; Miyoshi, S.; Tsuchiya, T.; Yamaguchi, S. Percolation conductivity in BaZrO<sub>3</sub>–BaFeO<sub>3</sub> solid solutions. *Solid State Ion.* **2014**, *126*, 875–878.

(28) Fabbri, E.; Markus, I.; Bi, L.; Pergolesi, D.; Traversa, E. Tailoring mixed proton-electronic conductivity of BaZrO<sub>3</sub> by Y and Pr co-doping for cathode application in protonic SOFCs. *Solid State Ion.* **2011**, *202*, 30–35.

(29) Antunes, I.; Amador, U.; Alves, A.; Rosario Correia, M.; Ritter, C.; Frade, J. R.; Perez-Coll, D.; Mather, G. C.; Fagg, D. P. Structure and Electrical-Transport Relations in Ba(Zr,Pr)O<sub>3-δ</sub> Perovskites. *Inorg. Chem.* **2017**, *56*, 9120–9131.

(30) Kasyanova, A. V.; Tarutina, L. R.; Rudenko, A. O.; Lyagaeva, J. G.; Medvedev, D. A. Ba(Ce,Zr)O<sub>3</sub>-based electrodes for protonic ceramic electrochemical cells: towards highly compatible functionality and triple-conducting behavior. *Russ. Chem. Rev.* **2020**, *89*, 667–692.

(31) Chen, C.; Chen, D. J.; Gao, Y.; Shao, Z. P.; Ciucci, F. Computational and experimental analysis of Ba<sub>0.95</sub>La<sub>0.05</sub>FeO<sub>3-δ</sub> as a cathode material for solid oxide fuel cells. *J. Mater. Chem. A* **2014**, *2*, 14154–14163.

(32) Raimondi, G. *Defect chemistry of mixed conducting perovskite: Interplay of protonic defects, oxygen vacancies and electron holes*, Ph.D. Thesis; Universitaet Stuttgart: Stuttgart, Germany, 2022.

(33) Shang, M.; Tong, J.; O'Hayre, R. A promising cathode for intermediate temperature protonic ceramic fuel cells: BaCo<sub>0.4</sub>Fe<sub>0.4</sub>Zr<sub>0.2</sub>O<sub>3-δ</sub>. *RSC Adv.* **2013**, *3*, 15769–15775.

(34) Raimondi, G.; Giannici, F.; Longo, A.; Merkle, R.; Chiara, A.; Hoedl, M. F.; Martorana, A.; Maier, J. X-ray Spectroscopy of (Ba,Sr,La)(Fe,Zn,Y)O<sub>3-δ</sub> Identifies Structural and Electronic Features Favoring Proton Uptake. *Chem. Mater.* **2020**, *32*, 8502–8511.

(35) Raimondi, G.; Longo, A.; Giannici, F.; Merkle, R.; Hoedl, M. F.; Chiara, A.; Sahle, C. J.; Maier, J. Electronic modifications in (Ba,La)(Fe,Zn,Y)O<sub>3-δ</sub> unveiled by oxygen K-edge X-ray Raman scattering. *J. Mater. Chem. A* **2022**, *10*, 8866–8876.

(36) Vračar, M.; Kuzmin, A.; Merkle, R.; Purans, J.; Kotomin, E. A.; Maier, J.; Mathon, O. Jahn-Teller distortion around Fe<sup>4+</sup> in Sr(Fe,Ti<sub>1-x</sub>)O<sub>3-δ</sub> from x-ray absorption spectroscopy, x-ray diffraction, and vibrational spectroscopy. *Phys. Rev. B* **2007**, *76*, No. 174107.

(37) Klementiev, K. V. XAFSmass, freeware: <https://zenodo.org/records/8010353>.

(38) Mathon, O.; Beteva, A.; Bugnazet, D.; Gatla, S.; Hino, R.; Kantor, I.; Mairs, T.; Munoz, M.; Pasternak, S.; Perrin, F.; Pascarelli, S. The time-resolved and extreme conditions XAS (TEXAS) facility at the European Synchrotron Radiation Facility: the general-purpose EXAFS bending-magnet beamline BM23. *J. Synchrotron Radiat.* **2015**, *22*, 1548–1554.

(39) Raimondi, G.; Merkle, R.; Maier, J. Impact of first-row transition metals in (Ba,La)(Fe,TM)O<sub>3-δ</sub> on proton uptake and electronic conductivity. *Solid State Ion.* **2023**, *391*, No. 116143.

(40) Uehara, H.; Ishii, A.; Oikawa, I.; Takamura, H. Preparation and mixed proton-hole conductivity of barium zirconate doped with scandium and cobalt. *Int. J. Hydrogen Energy* **2022**, *47*, S577–S584.

(41) Longo, A.; Giannici, F.; Balerna, A.; Ingrao, C.; Deganello, F.; Martorana, A. Local Environment of Yttrium in Y-Doped Barium Cerate Compounds. *Chem. Mater.* **2006**, *18*, 5782–5788.

(42) Bjørheim, T. S.; Hoedl, M. F.; Merkle, R.; Kotomin, E.; Maier, J. Proton, Hydroxide Ion, and Oxide Ion Affinities of Closed-Shell Oxides: Importance for the Hydration Reaction and Correlation to Electronic Structure. *J. Phys. Chem. C* **2019**, *124*, 1277–1284.

(43) Zohourian, R.; Merkle, R.; Maier, J. Bulk Defect Chemistry of PCFC Cathode Materials: Discussion of Defect Interactions. *ECS Trans.* **2017**, *77*, 133–138.

(44) Mizusaki, J.; Mima, Y.; Yamaguchi, S.; Fueki, K.; Tagawa, H. Nonstoichiometry of the perovskite-type oxides La<sub>1-x</sub>Sr<sub>x</sub>CoO<sub>3-δ</sub>. *J. Solid State Chem.* **1989**, *80*, 102–111.

(45) Hoedl, M. F.; Ertural, C.; Merkle, R.; Dronskowski, R.; Maier, J. The Orbital Nature of Electron Holes in BaFeO<sub>3</sub> and Implications for Defect Chemistry. *J. Phys. Chem. C* **2022**, *126*, 12809–12819.

(46) Mueller, D. N.; De Souza, R. A.; Brendt, J.; Samuelis, D.; Martin, M. Oxidation states of the transition metal cations in the highly nonstoichiometric perovskite-type oxide Ba<sub>0.1</sub>Sr<sub>0.9</sub>Co<sub>0.8</sub>Fe<sub>0.2</sub>O<sub>3-δ</sub>. *J. Mater. Chem.* **2009**, *19*, 1960–1963.

(47) Hong, W. T.; Stoerzinger, K. A.; Lee, Y. L.; Giordano, L.; Grimaud, A.; Johnson, A. M.; Hwang, J.; Crumlin, E. J.; Yang, W.; Shao-Horn, Y. Charge-transfer-energy-dependent oxygen evolution reaction mechanisms for perovskite oxides. *Energy Environ. Sci.* **2017**, *10*, 2190–2200.

(48) Stauffer, D.; Aharony, A. *Introduction to Percolation Theory*; Taylor & Francis: London, **2018**.

(49) Nomura, K.; Kageyama, H. Transport properties of Ba(Zr<sub>0.8</sub>Y<sub>0.2</sub>)O<sub>3-δ</sub> perovskite. *Solid State Ion.* **2007**, *178*, 661–665.

(50) Mizusaki, J.; Sasamoto, T.; Cannon, W. R.; Bowen, H. K. Electronic Conductivity, Seebeck Coefficient, and Defect Structure of La<sub>1-x</sub>Sr<sub>x</sub>FeO<sub>3</sub> (x = 0.1, 0.25). *J. Am. Ceram. Soc.* **1983**, *66*, 247–252.

(51) Patrakeeve, M. V.; Leonidov, I. A.; Kozhevnikov, V. L.; Kharton, V. V. Ion–electron transport in strontium ferrites: relationships with structural features and stability. *Solid State Sci.* **2001**, *6*, 907–913.

(52) Jung, J. I.; Mixture, S. T.; Edwards, D. D. The electronic conductivity of Ba<sub>0.5</sub>Sr<sub>0.5</sub>Co<sub>x</sub>Fe<sub>1-x</sub>O<sub>3-δ</sub> (BSCF: x = 0 ~ 1.0) under different oxygen partial pressures. *J. Electroceram.* **2010**, *24*, 261–269.

(53) Patrakeeve, M. V.; Mitberg, E. B.; Lakhtin, A. A.; Leonidov, I. A.; Kozhevnikov, V. L.; Kharton, V. V.; Avdeev, M.; Marques, F. M. B. Oxygen Nonstoichiometry, Conductivity, and Seebeck Coefficient of La<sub>0.3</sub>Sr<sub>0.7</sub>Fe<sub>1-x</sub>Ga<sub>x</sub>O<sub>2.65+δ</sub> Perovskites. *J. Solid State Chem.* **2002**, *167*, 203–213.

(54) Medarde, M.; Mesot, J.; Lacorre, P.; Rosenkranz, S.; Fischer, P.; Gobrecht, K. High-pressure neutron-diffraction study of the metallization process in PrNiO<sub>3</sub>. *Phys. Rev. B* **1995**, *52*, 9248–9258.

(55) Radaelli, P. G.; Iannone, G.; Marezio, M.; Hwang, H. Y.; Cheong, S. W.; Jorgensen, J. D.; Argyriou, D. N. Structural effects on the magnetic and transport properties of perovskite A<sub>1-x</sub>A'<sub>x</sub>MnO<sub>3</sub> (x = 0.25, 0.30). *Phys. Rev. B* **1997**, *56*, 8265–8276.

(56) Salamon, M. B.; Jaime, M. The physics of manganites: Structure and transport. *Rev. Mod. Phys.* **2001**, *73*, 583–628.

(57) Marthinsen, A.; Wahnstrom, G. Percolation Transition in Hole-Conducting Acceptor-Doped Barium Zirconate. *Chem. Mater.* **2020**, *32*, 5558–5568.

- (58) Rothschild, A.; Menesklou, W.; Tuller, H. L.; Ivers-Tiffée, E. Electronic Structure, Defect Chemistry, and Transport Properties of  $\text{SrTi}_{1-x}\text{Fe}_x\text{O}_{3-y}$  Solid Solutions. *Chem. Mater.* **2006**, *18*, 3651–3659.
- (59) Nomura, K.; Kageyama, H. Transport properties of  $\text{Ba}(\text{Zr}_{0.8}\text{Y}_{0.2})\text{O}_{3-\delta}$  perovskite. *Solid State Ion.* **2007**, *178*, 661–665.
- (60) Rao, Y.; Zhong, S.; He, F.; Wang, Z.; Peng, R.; Lu, Y. Cobalt-doped  $\text{BaZrO}_3$ : A single phase air electrode material for reversible solid oxide cells. *Int. J. Hydrogen Energy* **2012**, *37*, 12522–12527.
- (61) Bohn, H. G.; Schober, T. Electrical Conductivity of the High-Temperature Proton Conductor  $\text{BaZr}_{0.9}\text{Y}_{0.1}\text{O}_{2.95}$ . *J. Am. Ceram. Soc.* **2000**, *83*, 768–772.
- (62) Kreuer, K. D. Aspects of the formation and mobility of protonic charge carriers and the stability of perovskite-type oxides. *Solid State Ion.* **1999**, *125*, 285–302.
- (63) Ahmed, I.; Eriksson, S.-G.; Ahlberg, E.; Knee, C. S.; Götlind, H.; Johansson, L.-G.; Karlsson, M.; Matic, A.; Börjesson, L. Structural study and proton conductivity in Yb-doped  $\text{BaZrO}_3$ . *Solid State Ion.* **2007**, *178* (2007), 515–520.
- (64) Maier, J. *Physical Chemistry of Ionic Materials*; Wiley, 2004.
- (65) Kilner, J. A.; Brook, R. J. A study of oxygen ion conductivity in doped non-stoichiometric oxides. *Solid State Ion.* **1982**, *6*, 237–252.
- ES
- (66) De Souza, R. A. Oxygen Diffusion in  $\text{SrTiO}_3$  and Related Perovskite Oxides. *Adv. Funct. Mater.* **2015**, *25*, 6326–6342.
- (67) Merkle, R.; Mastrikov, Y. A.; Kotomin, E. A.; Kuklja, M. M.; Maier, J. First Principles Calculations of Oxygen Vacancy Formation and Migration in  $\text{Ba}_{1-x}\text{Sr}_x\text{Co}_{1-y}\text{Fe}_y\text{O}_{3-\delta}$  Perovskites. *J. Electrochem. Soc.* **2011**, *159*, B219–226.
- (68) Radaelli, P. G.; Iannone, G.; Marezio, M.; Hwang, H.-Y.; Cheong, S.-W.; Jorgensen, J. D.; Argyriou, D. N. Structural effects on the magnetic and transport properties of perovskite  $\text{A}_{1-x}\text{A}'_x\text{MnO}_3$  ( $x = 0.25, 0.30$ ). *Phys. Rev. B* **1997**, *56*, 8265–8276.
- (69) Cammarata, A.; Rondinelli, J. M. Covalent dependence of octahedral rotations in orthorhombic perovskite oxides. *J. Chem. Phys.* **2014**, *141*, 114704.
- (70) Zhang, Y.; Schmitt, M. M.; Mercy, A.; Wang, J.; Ghosez, P. From charge- to orbital-ordered metal-insulator transition in alkaline-earth ferrites. *Phys. Rev. B* **2018**, *98*, 081108(R).